Iraqi Journal of Physics, 2020 *Vol.18, No.44, PP. 69-84*
DOI: 10.20723/ijp.18.44.69-84

Study of the nuclear structure for ^{38}Ar, ^{59}Co, ^{124}Sn, ^{146}Nd, ^{153}Eu and ^{203}Tl target nuclei used in fabrication the nuclear batteries

Samaa S. Nassir and Ali A. Alzubadi

Department of Physics, College of Science, University of Baghdad, Baghdad, Iraq

E-mail: ali.a.alzubadi@scbaghdad.edu.iq

Abstract

The nuclear structure of ^{40}Ar, ^{112}Cd, ^{133}Cs, ^{151}Eu, ^{154}Sm, and ^{226}Ra target nuclei used in nuclear battery technology has been investigated in the framework of Hartree-Fock approximation based on Skyrme effective two-body interaction. These nuclei are extensively used in radioisotope thermo-electric generator space studies and for beta voltaic battery microelectronic systems. For this purpose, some static nuclear properties have been calculated. In particular, the various nuclear single particle radial density distribution, the corresponding root mean square radii, neutron skin thicknesses and binding energies. The bremsstrahlung spectrums produced by absorption of beta particles in beta voltaic process and the backscattered photon spectrum have also been calculated. All obtained results are compared with available experimental data.

Key words
Skyrme-Hartree-Fock, nuclear batteries, bremsstrahlung spectrum.

Article info.
Received: Nov. 2019
Accepted: Dec. 2019
Published: Mar. 2020

دراسة التركيب النووي لـ ^{38}Ar, ^{59}Co, ^{124}Sn, ^{146}Nd, ^{153}Eu و ^{203}Th أنوية الهدف المستخدمة في تصنيع البطاريات النووية

سماء سمير ناصر و علي عبد اللطيف كريم

قسم الفيزياء، كلية العلوم، جامعة بغداد، بغداد، العراق

الخلاصة

تم دراسة التركيب النووي لـ ^{38}Ar, ^{59}Co, ^{124}Sn, ^{146}Nd, ^{153}Eu و ^{203}Th أنوية الهدف المستخدمة في تكنولوجيا البطاريات النووية في إطار تقريب هارتري-فوك والمستند إلى تفاعل سكيرم الفعال بين الجسمين. هذه النوى تستخدم على نطاق واسع بالدراسات الفضائية للمولدات المشعة بالكهرباء الحرارية والنظم الإلكترونية الدقيقة للبطاريات بيتافوليتيك. لهذا الغرض، قمنا بحساب مختلف توزيع كثافة شعاعي الجسيمات أحادية النووية، يعني الجذر التربيعي المقابلة نصف قطرها مربع، سمك الجلد النيوتروني والطاقات ملزمة. كما تم حساب طيف أشعة الكبح الناتج عن امتصاص جسيمات بيتا في عملية بيتافوليتيك وطيف الفوتون المرتد. تتمت مقارنة جميع النتائج التي تم الحصول عليها مع البيانات التجريبية المتاحة.

Introduction

Because of the growing use as a long-life source of energy, nuclear batteries have a significant position in technology, particularly in space-craft and microelectronic applications nuclear batteries convert thermal energy from the decay of radioactive material into electricity [1, 2]. There are two main types of nuclear batteries, thermal converting and non-thermal converting such as betavoltaics [3]. This type of batteries converts energy disintegration into electricity via p-n junctions using semiconductor devices. Due to the greater densities of energy and the longer radioisotope life relative to another type [4]. Metavolcanics are used as a power supply in medical

purposes and microelectronic applications [5].

For this purpose, the nuclear static properties of some target nuclei used for production radioactive nuclei used in nuclear batteries namely; ^{38}Ar, ^{59}Co, ^{124}Sn, ^{146}Nd, ^{153}Eu and ^{203}Tl have been calculated in the framework of Hartree-Fock (HF) Approximation with Skyrme type Interaction. In particular, charge, proton, mass and neutron densities with their associated rms radii, nuclear binding energy and neutron skin. thickness have been calculated. The simulation of bremsstrahlung emission by beta particles using numerical cross-section and backscattered photons will be calculated.

Theoretical framework

The microscopic Mean-Field (MF) methods have been great used in studying the ground state nuclear properties of stable as well as the unstable nuclei. In this, context the tow-body effective interaction of Skyrme [6] and Gogny [7] are most often used with the non-relativistic HF method. The analytic simplicity of the Skyrme interaction allows for the definition of model parameters, which integrate basic nuclear properties [8].

In the literature, there are various Skyrme forces in the literature to evaluate nuclear properties; however, there are different numerical values for parameterizations of each force interaction [9, 10]. In the present work we used the SkM* parameterization, the Skyrme force is given with its numerical value in Table 1 [11]. The SkM* parameterization in the actinide region has been adapted to fission obstacles and surface tension. SkM* is an expanded version of SkM for big deformations and for astrophysical purposes could be used such as calculations of neutron stars [12].

Table 1: Skyrme parameterization used in the present calculations.

Parameters	SKM*
t_0 (MeV fm^3)	-2645.00
t_1 (MeV fm^5)	410.00
t_2 (MeV fm^5)	-135.00
t_3 (MeV fm^5)	15595
x_0	0.090
x_1	0.000
x_2	0.000
x_3	0.000
α	$1/6$
t_4 (MeV fm^5)	130

The Skyrme Hartree-Fock (SHF) equation is derived from the variation principle of the nucleus ground state wave function, which is considered to be a Slater determinant of the single particle state φ_β:

$$\varphi_\beta(x_1, x_2, \dots, x_A) = \frac{1}{\sqrt{A!}} det\left| \varphi_\beta(x_j)\right| \quad (1)$$

where x is the set of space $(\vec{r})$, spin (σ) and isospin coordinate (q), A is the number of sets and x_j is an all sets. The expectation value for the total Hamiltonian (H) of Slater determinant can be written as the integral of the Hamiltonian density H:

$$\langle\varphi|H|\varphi\rangle = \int H\,(\vec{r})d\vec{r} \quad (2)$$

For the Skyrme interaction, the Hamiltonian density is given as a function of the nucleon density (ρ_q), kinetic energy density (τ_q), and spin-orbit density $(\vec{J}_q)$, where q is proton or neutron. It can be written as the a sum of terms associated with different parts of the force [13]:

$$H = H_{kin} + H_0 + H_3 + H_{eff} + H_{fin} + H_{so} + H_{sg} + H_{coul} \quad (3)$$

where H_{kin} is the kinetic energy term, H_0 is zero range term, H_3 density dependent term, H_{eff} is an effected mass term, H_{fin} finite range term, H_{so} is a spin-orbit term, H_{sg} is the tensor coupling with spin and gradient term and H_{Coul} is a Coulomb term.

The terms in Eq. (3) are defined as follows [13]:

$$H_{kin} = \frac{\hbar^2}{2m}\tau$$

$$H_0 = \frac{t_0}{2}\left(1+\frac{x_0}{2}\right)\rho^2 - \frac{t_0}{2}\left(x_0+\frac{1}{2}\right)\sum_q \rho_q^2$$

$$H_3 = \frac{t_3}{12}\left(1+\frac{x_3}{2}\right)\rho^{2+\alpha} - \frac{t_3}{12}\left(x_3+\frac{1}{2}\right)\rho^{\alpha}\sum_q \rho_q^2$$

$$H_{eff} = \frac{1}{4}\left(t_1\left(1+\frac{x_1}{2}\right)+t_2\left(1+\frac{x_2}{2}\right)\right)\rho\tau - \frac{1}{4}\left(t_1\left(x_1+\frac{1}{2}\right)-t_2\left(x_2+\frac{1}{2}\right)\right)\sum_q \rho_q\tau_q$$

$$H_{fin} = \frac{1}{16}\left(3t_1\left(1+\frac{x_1}{2}\right)-t_2\left(1+\frac{x_2}{2}\right)\right)(\nabla\rho)^2 - \frac{1}{16}\left(t_1\left(x_1+\frac{1}{2}\right)+t_2\left(x_2+\frac{1}{2}\right)\right)\sum_q (\nabla\rho_q)^2$$

$$H_{so} = \frac{t_4}{2}\left(\overrightarrow{J}\cdot\nabla\rho + \sum_q \vec{J}_q\cdot\nabla\rho_q\right)$$

$$H_{sg} = -\frac{1}{16}(t_1x_1+t_2x_2)\vec{J}^2 + \frac{1}{16}(t_1-t_2)\sum_q \vec{J}_q^2$$

$$H_{coul} = \frac{e^2}{2}\rho_p(\vec{r})\int\frac{\rho_p(\vec{r}')}{|\vec{r}-\vec{r}'|}\overrightarrow{dr}' - \frac{3e^2}{4}\left(\frac{3}{\pi}\right)^{1/3}\rho_p^{4/3}(\vec{r}) \quad (4)$$

where H_{Coul} consists of the direct and exchange contributions and $t_0, t_1, t_2, t_3, x_0, x_1, x_2, x_3, \alpha \text{ and } t_4$ are the Skyrme parameterizations which are usually determined by fitting the experimental ground state properties of the spherical nuclei. The $\rho_q, \tau_q \text{ and } J_q$ are the densities distribution, kinetic energy density and spin-orbit density for the nucleon respectively. The non-indexed quantities represent the total density [14]:

$\rho = \rho_p + \rho_n$; $\tau = \tau_p + \tau_n$; $\vec{J} = \overrightarrow{J_p} + \overrightarrow{J_n}$. These densities are calculated from the single particle wave function φ_β defining the Slater determinant:

$$\rho_q(\vec{r}) = \sum_{\sigma,\beta}\left|\varphi_\beta(\vec{r},\sigma,q)\right|^2 \quad (5a)$$

$$\tau_q(\vec{r}) = \sum_{\sigma,\beta}\left|\nabla\varphi_\beta(\vec{r},\sigma,q)\right|^2 \quad (5b)$$

$$\overrightarrow{J_q}(\vec{r}) = (-i)\sum_{\sigma,\beta,\sigma'}\varphi^*_\beta(\vec{r},\sigma,q)\left[\nabla\varphi'_\beta(\vec{r},\sigma,q)\right]\times\langle\sigma|\vec{\sigma}|\sigma'\rangle \quad (5c)$$

The SHF equation is obtained by writing that the total energy E is stationary with respect to the variation of the single particle state, φ_β with the subsidiary condition that φ_β are normalized:

$$\frac{\delta}{\delta\varphi_\beta}E - \sum_\beta \in_\beta \int\left|\varphi_\beta(\vec{r})\right|^2 d\vec{r} = 0 \quad (6)$$

using the explicit from of the Hamiltonian density in Eq. (3), one can derive the equation for the single particle wave function φ_β:

$$\left[-\nabla\frac{\hbar^2}{2m^*_q(\vec{r})}\nabla + U_q(\vec{r}) - i\overrightarrow{W_q}(\vec{r}).(\nabla\times\sigma)\right]\varphi_\beta = \in_\beta \varphi_\beta \quad (7)$$

where $\overrightarrow{W_q}$ is a spin-orbit potential, σ is Pauli's matrix, q is the charge of the single-particle state β and the single particle wave function φ_β containing all the quantum effect of the system. Eq. (7) has a form of local Schrödinger equation with an effective mass $m^*_q(\vec{r})$ depends on density only [13]:

$$\frac{\hbar^2}{2m^*_q(\vec{r})} = \frac{\hbar^2}{2m} + \frac{1}{8}\left[t_1\left(1+\frac{x_1}{2}\right) + t_2\left(1+\frac{x_2}{2}\right)\right]\rho - \frac{1}{8}\left[t_1\left(x_1+\frac{1}{2}\right) + t_2\left(x_2+\frac{1}{2}\right)\right]\rho_q \quad (8)$$

whereas the central potential depends on kinetic energy density

$$U_q = t_0\left(1+\frac{x_0}{2}\right)\rho - t_0\left(x_0+\frac{1}{2}\right)\rho_q + \frac{t_3}{12}\rho^\alpha\left[(2+\alpha)\left(1+\frac{x_3}{2}\right)\rho - 2\left(\frac{1}{2}+x_3\right)\rho_q - \alpha\left(\frac{1}{2}+x_3\right)\frac{\rho_p+\rho_n}{\rho}\right] + \frac{1}{4}\left[t_1\left(1+\frac{x_1}{2}\right) - t_2\left(1+\frac{x_2}{2}\right)\right]\tau - \frac{1}{4}\left[t_1\left(x_1+\frac{1}{2}\right) - t_2\left(x_2+\frac{1}{2}\right)\right]\tau_q - \frac{1}{8}\left[3t_1\left(1+\frac{x_1}{2}\right) - t_2\left(1+\frac{x_2}{2}\right)\right]\nabla^2\rho + \frac{1}{8}\left[3t_1\left(x_1+\frac{1}{2}\right) + t_2\left(x_2+\frac{1}{2}\right)\right]\nabla^2\rho_q + \frac{1}{8}(t_1-t_2)\vec{J}_q - \frac{1}{8}(x_1t_1 - x_2t_2)\vec{J} + \delta_{q.proton}U_{Coul} \quad (9)$$

The spin-orbit potential is given by [13]:

$$\overrightarrow{W_q} = \frac{t_4}{2}\left(\nabla\rho + \nabla\rho_q\right) \quad (10)$$

and the Coulomb potential, where the exchange part is calculated with Slater approximations has a form of [15]:

$$U_{Coul} = \frac{e^2}{2}\int\frac{\rho_p(\vec{r}')}{|\vec{r}-\vec{r}'|}\overrightarrow{dr'} - e^2\left(\frac{3}{\pi}\right)^{1/3}\rho_p^{1/3}(\vec{r}) \quad (11)$$

Calculations method

The HF equations Eq. (7) is solved self-consistently to obtain the desired wave function for single-particle state, φ_β. After the wave function is obtained the binding energy of nucleus is calculated according to Eq. (2). The densities and local potential are then evaluated using Eqs. (5 and 9), respectively. In performing the calculations, we use the computer code for spherical SHF+BCS [16] where the contribution of pairing interaction to the binding energy of the nucleus is calculated as:

$$E_{pair} = -\sum_q G_q\left[\sum_{\beta\in q}\sqrt{\omega_\beta(1-\omega_\beta)}\right]^2 \quad (12)$$

where the pairing matrix elements (G_q) are constant within each species $q \in \{p,n\}$. The occupation probability (ω_β) is determined by solving the Bardeen–Cooper–Schrieffer (BCS) pairing equation:

$$\omega_\beta = \frac{1}{2}\left[1 - \frac{\epsilon_\beta - \epsilon_{F,\beta}}{\sqrt{(\epsilon_\beta - \epsilon_{F,\beta})^2 + \Delta_q^2}}\right] \quad (13)$$

The pairing gap (Δ_q) and the Femi energy ($\epsilon_{F,\beta}$) are determined by simultaneous solution of the gap equation and the particle number condition:

$$\frac{\Delta_q}{G_q} = \sum_{\beta\epsilon q}\sqrt{\omega_\beta(1-\omega_\beta)} \;\; ; \;\; A_q = \sum_{\beta\epsilon q}\omega_\beta \quad (14)$$

where A_q is the desired number of protons and neutrons. In solving Eq.(13) we use a constant gap approach for proton and neutron:

$$\Delta_p = \Delta_n = \frac{11.2}{\sqrt{A}} MeV \quad (15)$$

where A is a nucleon number.

The rms radii of proton, charge, neutron and mass distributions can be evaluated from these densities as [17]:

$$r_q = \langle r_q^2\rangle^{1/2} = \left[\frac{\int \vec{r}^2 \rho_q(\vec{r})\, d\vec{r}}{\int \rho_q(\vec{r})\, d\vec{r}}\right]^{1/2} \quad (16)$$

The neutron thickness can be given as [18]:

$$t_n = r_n - r_p \quad (17)$$

where r_n is the rms of neutron and r_p is the rms of proton.

The cross section $\sigma(W_e, k)$ for the production of bremsstrahlung photon of energy between k and $+dk$, Integrated by an electron with total energy W_0 in all photon directions (including rest-mass energy m_0c^2) when it interacts with the Coulomb field of target nucleus of atomic number Z and atomic mass A. The expression for the cross section is given by [19-21]:

$$\sigma(W_e,k) = \frac{Z^2 r_\circ^2}{137}\frac{dk}{k}\frac{P}{P_e}\left\{\frac{4}{3} - 2W_eW\,\frac{P_e^2+P^2}{P_e^2+P^2} + \frac{\epsilon_e W}{P_e^3} + \frac{\epsilon W_e}{P^3} - \frac{\epsilon_e \epsilon}{P_\circ P} + L\left[\frac{8}{3}\frac{W_eW}{P_eP} + \frac{k^2(W_e^2\,W^2+P_e^2\,P^2)}{P_e^3\,P^3} + \frac{k}{2P_eP}\left(\frac{W_eW+P_e^2}{P_e^3}\epsilon_e - \frac{W_eW+P^2}{P^3}\epsilon + \frac{2kW_eW}{P_e^2P^2}\right)\right]\right\} \quad (18)$$

where r_0 is the classical electron radius $=e^2/m_o\,c^2 = 2.818\times10^{-3}cm$, W_e, P_e and W, P are the initial and final values of electron energy and momentum in units of m_0c^2 and m_0c, respectively, and k is the photon energy in m_oc^2 units.

The energy of the backscatter peak will give by:

$$E_{b.s} = E_\gamma - E_c = \frac{E_\gamma}{1+\frac{2E_\gamma}{m_oc^2}}\;(MeV) \quad (19)$$

where $E_{b.s}$ is backscattering energy, E_γ is gamma energy and E_c is Compton energy.

Results and discussion

The main concern of the present work is to calculate the most common nuclear static properties for some selected target nuclei used for production the pure beta emitter used in fabrication the nuclear batteries. The discussion of results for the nuclear structure will divided into two parts as follows; the first one is the most nuclear ground state features, for ^{38}Ar, ^{59}Co, ^{124}Sn, ^{146}Nd, ^{153}Eu and ^{203}Tl nuclei, have been studied within framwork of the HF method with SkM* Skyrme parameterization. The second one is the bremsstrahlung spectrum and backscattered photons for radioactive nuclei namely ^{39}Ar, ^{60}Co, ^{125}Sb, ^{147}Pm, ^{154}Eu and ^{204}Tl produced by the (n,γ) reaction on the target nuclei Table 2.

Table 2: The target nuclei used for production the pure β^- emitters for fabrication the nuclear batteries.

Target nuclei	Z	N	Decay energy (MeV)	Reaction	Product nuclei	β_{max} (MeV)
^{38}Ar	18	20	0.565	(n,γ)	^{39}Ar	0.565
^{59}Co	27	32	2.824	(n,γ)	^{60}Co	0.318
^{124}Sn	50	74	0.767	(n,γ)	^{125}Sb	0.302
^{146}Nd	60	86	0.225	(n,γ)	^{147}Pm	0.225
^{153}Eu	63	90	1.969	(n,γ)	^{154}Eu	1.845
^{203}Tl	81	122	0.763	(n,γ)	^{204}Tl	0.763

1. Charge, proton, neutron and mass density distributions

An investigation of the charge, proton, neutron and density mass distributions for ^{38}Ar, ^{59}Co, ^{124}Sn, ^{146}Nd, ^{153}Eu and ^{203}Tl nuclei have been performed on the HF with Skyrme force parameter SkM*. The calculated results were shown in Fig. 1 as a function of radius. For distinguishing between the various nuclear densities of each nucleus we used different colors. The calculated nuclear density profiles reveal that, with increasing mass, the density at the center of an atomic nucleus decreases slightly, it means that as the mass number of each nucleus increases, the central density becomes less dense with increasing volume and radius [22]. The charge density distributions were obtained by folding the charge distributions of a proton with the density of the proton determined using the HO wave as the formula below

$$R^c_{rmc} = \left[\left(R^p_{rmc}\right)^2 + (0.8)^2\right]^{1/2} \; fm$$

where 0.8 fm is the rms charge radius of a proton [11].

In computing the observable charge densities using SHF method, another fact should also be considered that the nucleons themselves have intrinsic electromagnetic structure. Thus one has to compute the proton, neutron and mass density of the nucleons. To illustrate the behavior of the one particle nuclear density distribution, the calculated charge, proton, neutron and mass densities of the target nuclei are depicted in Figs. 1. Different colors are used to differentiate between the different nucleons nuclear densities.

In general point of view, we can deduce that in the case of heavy nuclei, the nuclear density is constant near the center and falls fairly rapidly to zero at the nuclear surface. Their neighbors, so that, when one adds a new particle to the system, most of the others are not directly affected by its presence. Thus, interior density does not substantially change by increasing the number of the value of ρ_0 is in the range of 0.05-0.18 fm^{-3} for medium to heavy nuclei and decreases slowly with increasing mass number.

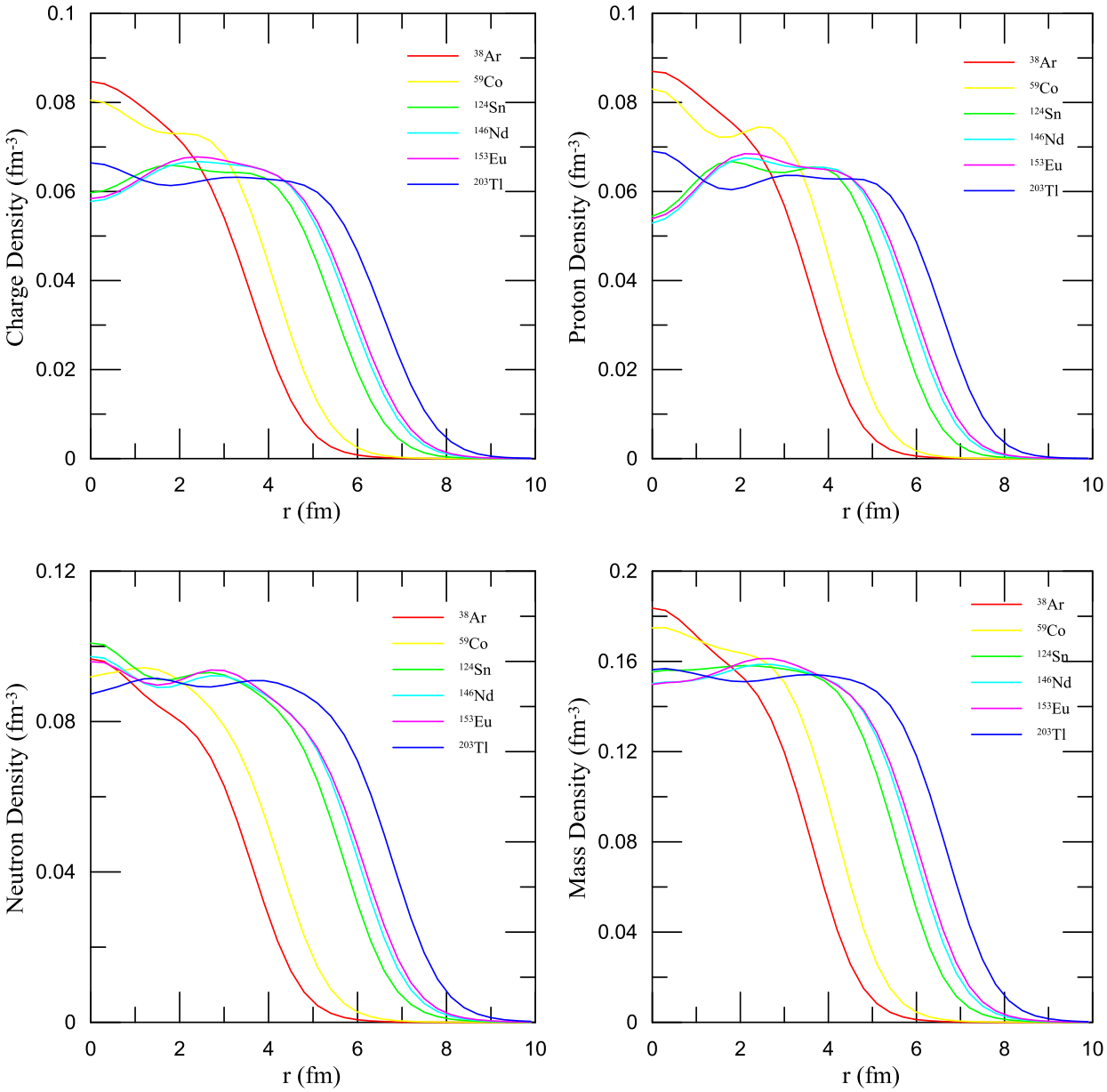

Fig.1: The calculated charge, proton, neutron and mass densities of the selected target nuclei using SkM* parameterization.

From these figures, it can be seen that the central nuclear densities gradually decrease as the nucleons number A increases, this is due to the change in the self-consistent HF potential coming from the additional nucleons. This change in charge density is available in the interior and the surface regions of the nuclei. The contribution of additional nucleons to the density is directly associated to the orbits that are filled. These orbits are changing the densities in the interior and the surface regions.

2. Root mean square radii

The calculated mass, neutron, proton and charge rms radii for the selected target nuclei are tabulated in Table 3 and depicted in Fig. 2. The theoretical charge rms radii are compared with the available experimental data taken from Ref. [23], but the experimental data of the rms proton, neutron and mass are missing in the literature.

Table. 3 The calculated mass, neutron, proton and charge rms radii (in fm) using SkM* Skyrme parameterization and compared with experimental data results taken from Ref. [23]

Nuclei	Mass	Neutron	Proton	Charge	Charge (Exp)	$t_n=r_n-r_p$
^{38}Ar	3.349	3.358	3.339	3.437	3.4028	0.019
^{59}Co	3.748	3.779	3.711	3.799	3.7875	0.068
^{124}Sn	4.726	4.798	4.618	4.688	4.6735	0.180
^{146}Nd	4.978	5.037	4.892	4.947	4.9696	0.145
^{153}Eu	5.056	5.115	4.970	5.023	5.1115	0.145
^{203}Tl	5.522	5.583	5.428	5.483	5.4666	0.155

It is obvious that, the calculated rms radii of charge, proton, mass and neutron with SkM* Skyrme parametrization for ^{38}Ar, ^{59}Co, ^{124}Sn, ^{146}Nd, ^{153}Eu and ^{203}Tl nuclei have increased with the increase of the mass number. The theoretical charge rms radii increasing from 3.437 for ^{38}Ar to 5.483 for ^{203}Tl and have a good agreement with experimental data.

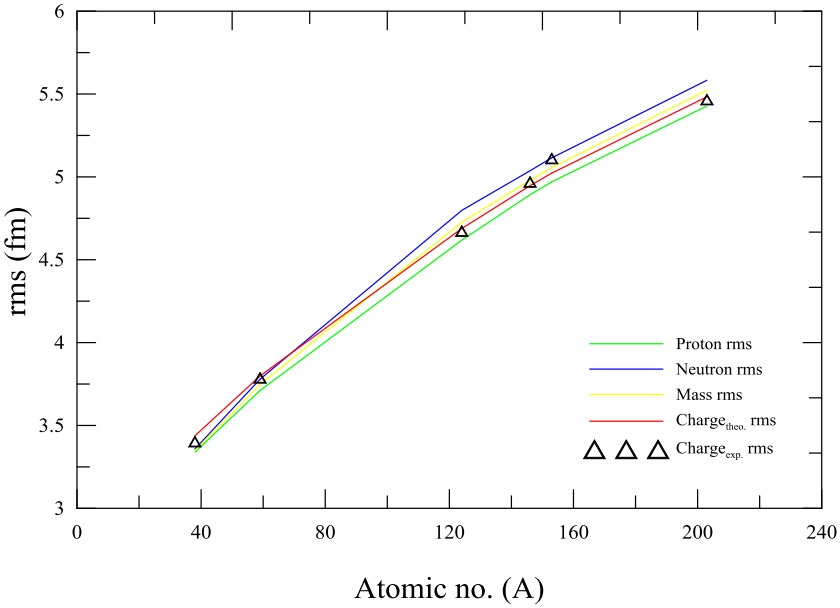

Fig.2: Rms for selected target nuclei calculated using SkM* Skyrme parameterization along with experimental data taken from Ref [23].

3. Neutron skin thickness

To determine neutron thicknesses, based on Eq. (17), the rms neutron and proton density radii were exploited in Table 2. Where the calculated neutron skin thickness *t*. The neutron thicknesses for the ^{38}Ar, ^{59}Co, ^{124}Sn, ^{146}Nd, ^{153}Eu and ^{203}Tl nuclei are given in the last column of Table 2 and displayed in Fig. 3. The theoretical t_n values are increase with increasing mass number. In the present work, the ^{124}Sn nucleus has the biggest values 0.180, and ^{38}Ar nucleus has the lowest value 0.019. Where, t is the difference between the neutron rms radius r_n and the proton rms radius r_p.

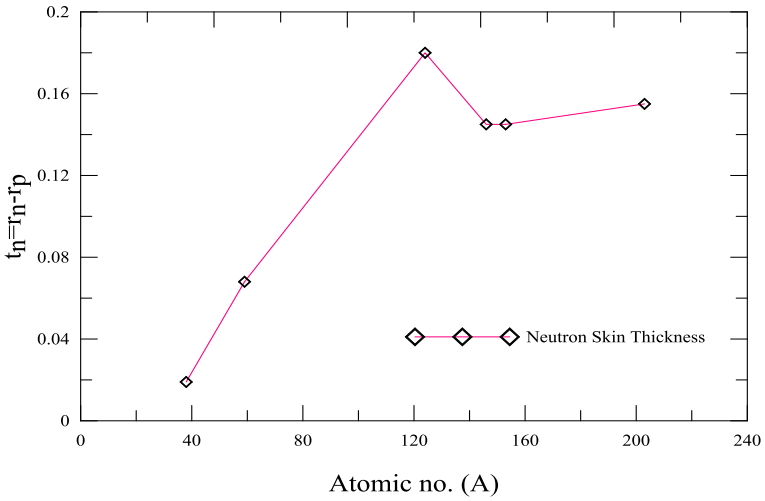

Fig 3: The neutron skin thickness for ^{38}Ar, ^{59}Co, ^{124}Sn, ^{146}Nd, ^{153}Eu and ^{203}Tl nuclei using SkM* Skyrme parameterization.

4. Binding energies

The calculated binding energies of the selected nuclei ^{38}Ar, ^{59}Co, ^{124}Sn, ^{146}Nd, ^{153}Eu and ^{203}Tl nuclei have been tabulated in Table 4 and compared with the experimental data taken from Ref. [24]. The results are also displayed graphically in Fig. 4. The both experimental results and theoretic al results of binding energies are depending on mass number, when the mass number increases the binding energy increases.

Table 4: The calculated binding energy using SkM* Skyrme parameterization in MeV and compared with experimental data results taken from ref. [24].

Nuclide	SkM*	Exp [24]
^{38}Ar	321.12	327.347
^{59}Co	509.75	517.321 ±0.001
^{124}Sn	1038.4	1049.980 ±0.001
^{146}Nd	1194.2	1212.423 ±0.002
^{153}Eu	1236.4	1259.018 ±0.002
^{203}Tl	1586.6	1600.898 ±0.002

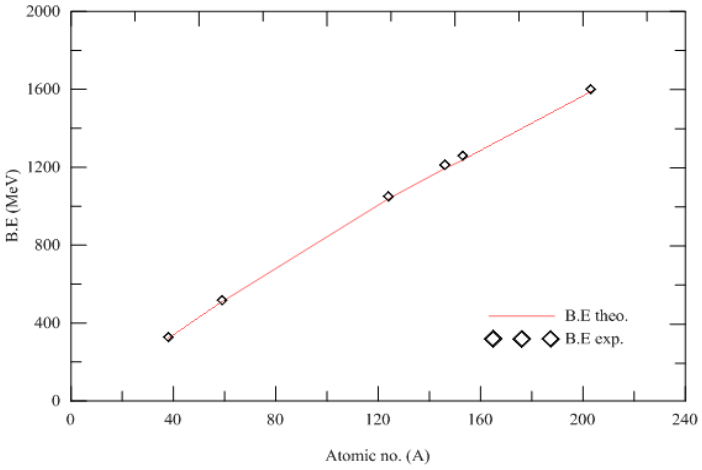

Fig.4: The calculated total binding energies for selected target nuclei calculated using the SHF method.

5. Cross - Sections for bremsstrahlung emission

In this section we will calculate the bremsstrahlung spectrum for radioactive nuclei ^{39}Ar, ^{60}Co, ^{125}Sb, ^{147}Pm, ^{154}Eu and ^{204}Tl that produced by absorption of beta particles in betavoltaic process. In nuclear battery designs, the choice of a suitable radioisotope with a suitable energy of the ionization radiation is very important. It is depending on the range of the energy emitted from the isotope in the material that the isotope is embedded in. For betavoltaic a p-n junction in a semiconductor is used as a transducer. Beta particles transfer energy to the target material by Coulomb scattering and bremsstrahlung emission [25]. Since the incident beta particles have a mass equal to the mass of the target electrons, their path of losses energy in a material will be random and significant scattering. Simulation of the beta particle tracks emitted from the pure beta emitters in silicon carbide (SiC) semiconductor have been investigated and illustrated in Fig. 5 using Mont Carlo code [26]. In these figures the yz section were the beam is coming parallel to the z-axis vertically down to the sample. The backscattering beta particles have been shown in these figures with a red path.

The generation of secondary gamma photons from bremsstrahlung events, produced by interaction of beta particles with the target nuclei, requires an additional shielding in battery design. Bremsstrahlung energy generation is effective when transducer material has a high atomic number, since its scales approximately as Z^2 of the target. In the present work, the SiC semiconductor has been used as a transducer material with relatively low atomic number. Fig. 6 shows the simulated bremsstrahlung spectra produced by beta particles impinging normally on the slab of SiC [27]. The comparison of the bremsstrahlung spectrums with different energies are shown in Fig. 7, It has been found that the probability density of the generated bremsstrahlung decreases with the increasing the bremsstrahlung energy.

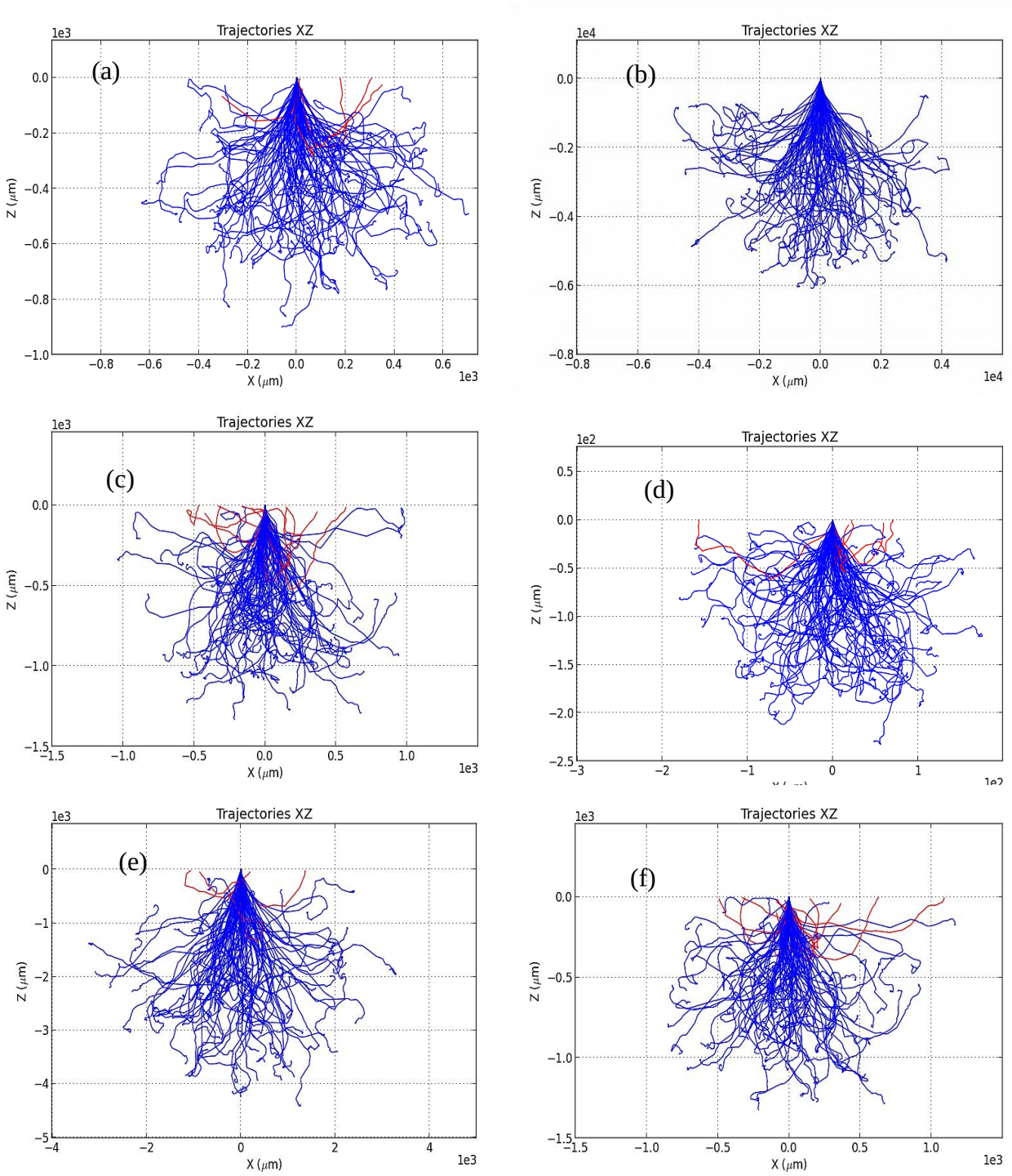

Fig.5: The trajectories of (a) ^{39}Ar, (b) ^{60}Co, (c) ^{125}Sb, (d) ^{147}Pm, (e) ^{154}Eu and (f) ^{204}Tl respectively beta particles into silicon carbide with the beam entering a slab. The blue lines: absorbed within the sample, the red lines: backscattered (beta particle exits from the same surface as it entered).

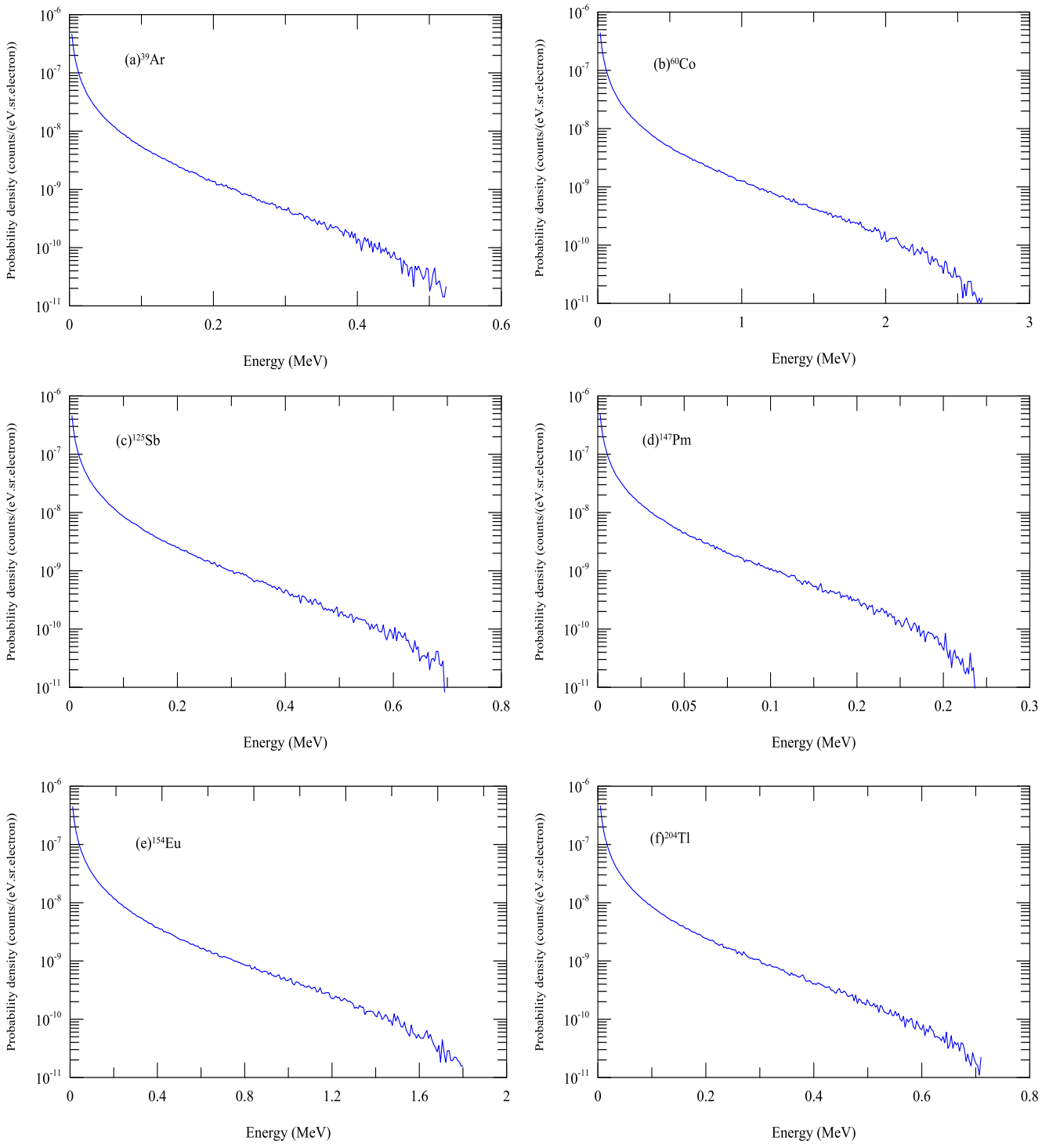

Fig.6: The bremsstrahlung spectrum produced by absorption of (a) ^{39}Ar, (b) ^{60}Co, (c) ^{125}Sb, (d) ^{147}Pm, (e) ^{154}Eu, and (f) ^{204}Tl beta particles into silicon carbide.

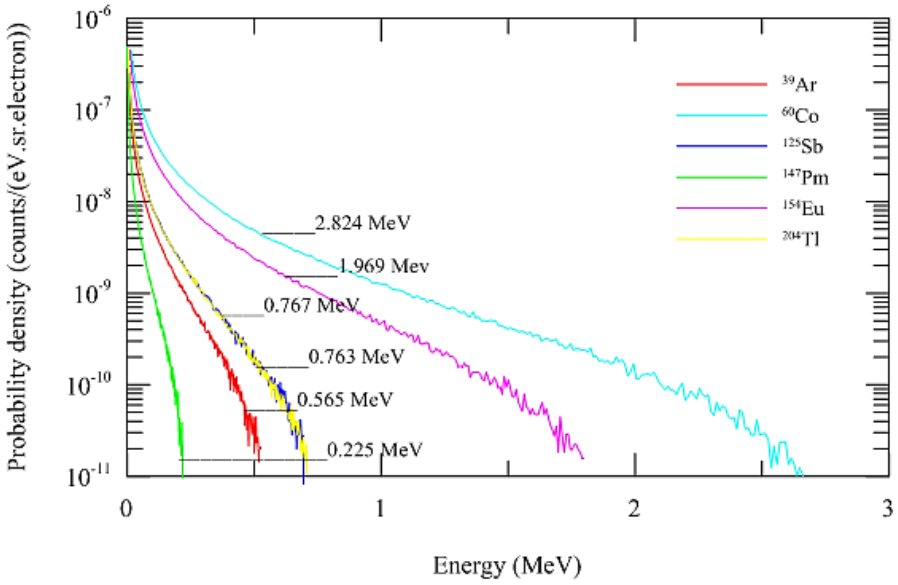

Fig.7: The comparison of the bremsstrahlung spectrums produced by absorption of target nuclei (^{39}Ar, ^{60}Co, ^{125}Sb, ^{147}Pm, ^{154}Eu and ^{204}Tl) beta particles into silicon carbide.

6. Backscattered photons spectrum

In the present work, a Monte Carlo code has been used to provide insight into gamma ray simulator result and backscattering probabilities simulation for the energy distributions and the backscattered probabilities of gamma photons of various energies, multiply backscattered from SiC semi-conductor used in nuclear batteries are presented. As is usual for detailed Monte Carlo calculations, a gamma photon is represented by its energy, position coordinate $(\theta, \emptyset)$, and direction cosines relative to some frame of reference. These quantities are chosen as randomly generated parameters with the selection of the processes (one of photoelectric or Compton) when an interaction occurs. The Code provides the energy distribution of backscattered photons after several scatterings in the semi-conductor.

The energy distribution of backscattered of bremsstrahlung photons produced by absorption of beta particles emitted from ^{39}Ar, ^{60}Co, ^{125}Sb, ^{147}Pm, ^{154}Eu and ^{204}Tl sources in 0.3 µm thickness of SiC were calculated and depicted in Fig. 8. For all sources, the energy distributions initially increases and reach a maximum value, thereafter, they decrease rapidly with increasing photons energy. Since the energy distributions occur in small energy region, a semi-logarithmic graph is down.

The backscattering energy distributions of gamma photons were calculated for different incident photon energies. The mechanism of interaction depends on the type of particle, energy and density. The results are shown in Fig. 9 for ^{39}Ar, ^{60}Co, ^{125}Sb, ^{147}Pm, ^{154}Eu and ^{204}Tl. The backscattering energy distributions show similar behavior. They have two clear peaks. It is considerable that the energy distributions of photons scattered backward from the various beta sources show peaks at approximately 0.00135-0.10015 MeV in the selected energy range. It is caused by Compton scattering in the material. The second maximum is the backscattering energy distributions occurs at different energy value compared to the other sources, probably due to the larger number of bremsstrahlung photons from higher energy beta source. As shown in

Fig. 9, the energy distributions of backscattering photons vary depending on the decrease in their probability of going forward through the SiC thickness. The peak positions of the backscattered photons are shifted to higher energies as the incident photon energy increases.

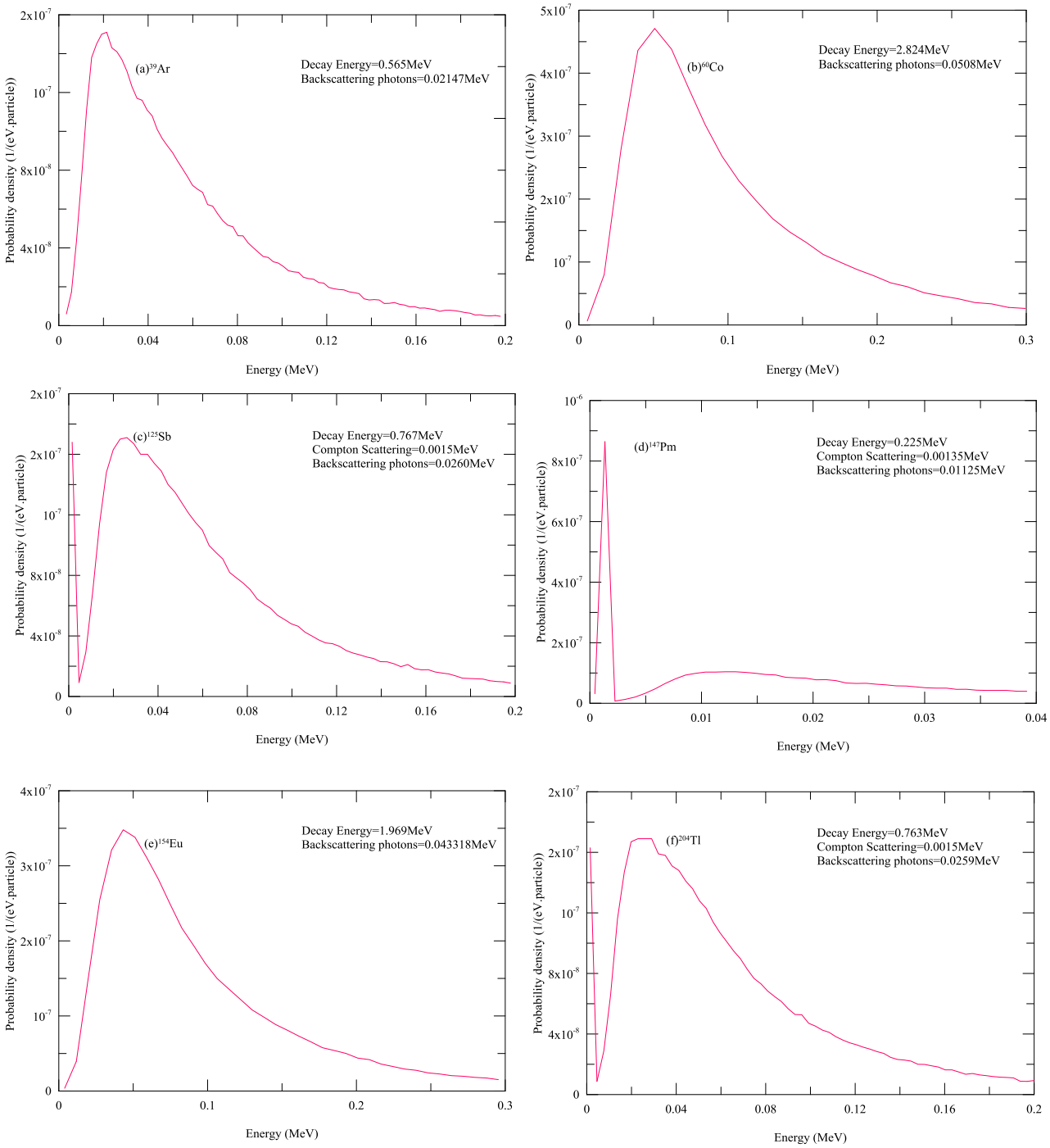

Fig.8: The backscattered of bremsstrahlung photons produced by absorption of (a) ^{39}Ar, (b) ^{60}Co, (c) ^{125}Sb, (d) ^{147}Pm, (e) ^{154}Eu, and (f) ^{204}Tl beta particles into silicon carbide.

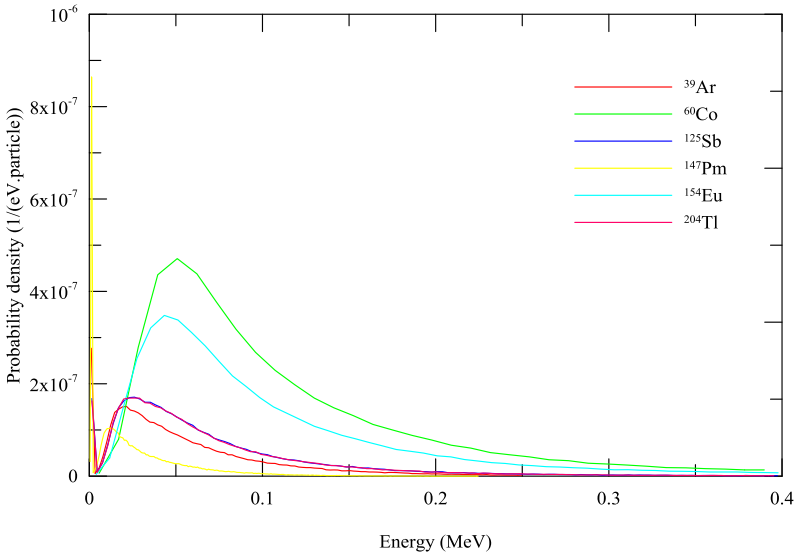

Fig.9: The backscattered photons spectrums produced by absorption of target nuclei (^{39}Ar, ^{60}Co, ^{125}Sb, ^{147}Pm, ^{154}Eu, and ^{204}Tl) beta particles into silicon carbide.

Conclusions

From the research that has been performed, it is possible to conclude that the binding energies and rms radii of the selected target nuclei calculated using the SHF method with SkM* parameterization are well reproduced and close to the experimental data. The SHF method is the useful for calculating of the spherical nuclei because this force is central and has zero range interactions. The intensity of bremsstrahlung photons produced by beta particles absorption in SiC has been investigated as a function of energy. It was observed the intensity increases with the increasing beta particle energies and the backscattering photons also increases. This method can be used for optimization of the configuration of radiation protection in fabrication the nuclear batteries and it also provides assistance to extend nuclear data used in nuclear battery technology and science.

References

[1] A. Khajepoura and F. Rahmani, Appl. Radiat. Isot., 119 (2017) 51-56.
[2] G. R. Schmidt, T. J. Sutli, L. A. Dudzinski, Radioisotope power: A key technology for deep space exploration in Radioisotopes Applications in Physical Sciences, ed. Nirmal Singh (2011), 419.
[3] A. Kavetsky, G. Yakubova, Q. Lin, D. Chan, S. M. Yousaf, K. Bower, J. D. Roberts, J. D. Robertson, A. Garnov, D. Meier, Appl. Radiat. Isot. 67 (2009) 1057-1062.
[4] D. Y. Qiao, X. J. Chen, Y. Ren, W. Z. Yuan, J. of Micro electro mechanical Systems, (2011) 685-690.
[5] E. B. Yakimov, Appl. Radiat. Isot., 112 (2016) 98-102.
[6] D. Vautherin and D.M. Brink, Phys. Rev., C 5 (1972) 626-630.
[7] J. Decharge and D. Gogny, Phys. Rev., C 21 (1980) 1568-1574.
[8] A. A. Alzubadi, Ind. J. Phys., 89 (2015) 619-627.
[9] A. A. Alzubadi, N. F. Latooffi, R. A. Radhi, Int. J. Mod. Phys., E 24, 12 (2015) 1550099.
[10] P. Ring and P. Schuck, "The Nuclear Many Body Problem" Springer (1980).
[11] E. Chabanat, P. Bonce, P. Haensel, J. Meyer, R. Schaefer, Nucl. Phys., A 627 (1997) 710-746.
[12] P. G. Reinhard and H. Flocard, Nucl. Phys., A 584 (1995) 467-488.

[13] E. Chabanat, P. Bonce, P. Haensel, J. Meyer, R. Schaefer, Nucl. Phys. A 635 (1998) 231-256.
[14] J. Bartel and K. Bencheikh, European Phys. J. A-Hadrons and Nuclei, 14 (2002) 179-190.
[15] J. G. Snijders and E. J. Baerends, Mol. Phys., 33 (1977) 1651-1662.
[16] P.G. Reihard, Berlin: Spring Verlag, 1 (1991) 28-33.
[17] H. Aytekin, E. tel, R. Baldik, A. Aydin, J. Fusion Energy, 30 (2011) 21-25.
[18] E. Tel, R. Baldik, H. Aytekin, A. Aydin, Ann. Nucl. Energy, 36 (2009) 1333-1341.
[19] K.V.N. Sarma and K. Narasimha Murty, J. Phys. G. Nucl. Phys., 2 (1976) 387-400.
[20] M. Takehisa, T. Saito, T. Takahashi, Y. Sato, T. Sato, Radiat. Phys. Chem., 42 (1993) 495-498.
[21] O. S. Uehara, S. Taniguchi, M. Kashiwagi, K. Mizusawa, I. Sakamoto Radiat. Phys. Chem., 42 (1993) 515-518.
[22] M. Sahan, E. Tel, H. Sahan, A. Kara, A. Aydin, A. Kaplan, I. H. Sarpun, B. Demir, S. Akca, E. Yildiz, J. of Fusion Energy, 3 (2015) 493-499.
[23] I. Angeli and K.P. Marinova, J. Atom. Nucl. Dat. Table 99 (2013).
[24] http://cdfe.sinp.msu.ru/services/.
[25] M.A. Prelas, C.L. Weaver, M.L. Watermann, E.D. Lukosi, R.J. Schott, D.A.Wisniewski, Nucl. Energy, 75 (2014) 117-148.
[26] D. W. O. Rogers, B. A. Faddegon, G. X. Ding, C.M. Ma, J. We, T. R. Mackie, Medical Phys., 22, 5 (1995) 503-524.
[27] E. Acosta, X. Llovet, F. Salvat, Appl. Phys. Lett., 80 (2002) 3228-3233.